A Single Electrode Organic Neuromorphic Device for Dopamine Sensing in Vivo

Federico Rondelli, Michele Di Lauro,* Gioacchino Calandra Sebastianaella, Anna De Salvo, Matteo Genitoni, Mauro Murgia, Pierpaolo Greco, Carolina Giulia Ferroni, Riccardo Viaro, Luciano Fadiga, and Fabio Biscarini

Organic Electronic platforms for biosensing are being demonstrated at a fast pace, especially in healthcare applications where the use of organic (semi-)conductive materials leads to devices that efficiently interface living matter. Nevertheless, interesting properties of organic (semi-)conductors are usually neglected in the development of (bio-)sensors. Among these, the non-linear response when operated under dynamic biasing conditions (i.e., with pulsed driving voltages), thus mimicking synaptic plasticity phenomena, offers promising and largely unexplored possibilities for bio-sensing. The artificial synaptic response's figures of merit reflect the composition of the surrounding environment and, ultimately, the ion concentration and dynamics at the organic (semi-)conductor/electrolyte interface. Therefore, new sensing strategies that rely on the effect of target analytes on the short-term plasticity response of Organic Neuromorphic Devices are being demonstrated. This work presents the development of a label-free Single Electrode Neuromorphic Device (SEND) specifically designed for in vivo real-time mapping of dopamine concentration. The device response is investigated as a function of the driving frequency, resulting in the determination of the optimal operational configuration for minimally invasive neuromorphic devices. It exhibits stable multi-parametric response in complex fluids, in brain's mechanical models and in vivo, enabling monitoring of local variations of dopamine concentration in the rat brain.

1. Introduction

Dopamine (DA) is a neurotransmitter of critical importance in mammalian central nervous system (CNS); it is synthesized and released by dopaminergic neurons, an ensemble of neurons mainly located at mesencephalic level, in regions identified as *substantia nigra pars compacta* (SNpC) and in the ventral tegmental area (VTA). From these native locations, dopaminergic neurons project to other brain regions along three main pathways: the nigrostriatal pathway, connecting SNpC to the dorsal striatum (i.e., the ensemble Caudate-Putamen - CPu) and the mesocortical and mesolimbic pathways, connecting the VTA to the cortex and the nucleus Accumbens (NAc), respectively.[1]

DA plays a pivotal role in the modulation of different circuits associated with reward, memory, learning, attention and motor control. Furthermore, the imbalance in extracellular DA levels is known to lead to pathological conditions such as depression, schizophrenia, psychosis

F. Rondelli, M. Di Lauro, G. Calandra Sebastianaella[+], A. De Salvo, M. Genitoni, M. Murgia, P. Greco, C. G. Ferroni, L. Fadiga, F. Biscarini
Center for Translational Neurophysiology of Speech and Communication
Fondazione Istituto Italiano di Tecnologia (IIT-CTNSC)
via Fossato di Mortara 17/19, Ferrara 44121, Italy
E-mail: michele.dilauro@iit.it

F. Rondelli, M. Di Lauro, P. Greco, R. Viaro, L. Fadiga
Sezione di Fisiologia Dipartimento di Neuroscienze e Riabilitazione
Università di Ferrara
via Fossato di Mortara 17/19, Ferrara 44121, Italy

M. Murgia
Istituto per lo Studio dei Materiali Nanostrutturati (CNR-ISMN)
National Research Council
via Gobetti 101, Bologna 40129, Italy

F. Biscarini
Dipartimento di Scienze della Vita
Università di Modena e Reggio Emilia
Via Campi 103, Modena 41125, Italy

**ADVANCED
SCIENCE NEWS**

www.advancedsciencenews.com

**ADVANCED
ELECTRONIC
MATERIALS**

www.advelectronicmat.de

and Parkinson's disease (PD), according to the brain regions in which such levels are unbalanced.[2,3] In the case of PD, a decrease in extracellular CPu DA levels, mainly due to DAergic neurodegeneration of the nigrostriatal pathway, leads to the peculiar motor symptomatology patients, i.e., akinesia, bradykinesia, resting tremor, rigidity and abnormalities in gait and posture. Many parkinsonian patients also display non motor symptoms such as sleep disturbance, depression, anxiety, cognitive impairment and autonomic dysfunctions. Nevertheless, motor symptoms onset is associated with the loss of 50% of DAergic neurons in the SNnpC and 80% decrease of CPu extracellular DA levels.[4] Upon these premises, envisioning strategies for real-time DA concentration level monitoring might be of utmost importance to follow both diseases development and efficacy of therapeutic approaches during the early stages of PD, where symptomatological evidence is absent or mild.

At physiological pH, DA is present in the CNS as a cationic catecholamine exhibiting a positive net charge.[5] In the literature, in vivo DA quantification is achieved by means of two major techniques: microdyalisis and electrochemical detection. Microdyalisis exhibits a high degree of invasiveness coupled with poor translation capability, since it relies on off-line analysis of the microdyalized sample by means of sophisticated expensive equipment. Electrochemical techniques, on the other hand, take advantage of the oxidation of DA at an electrode interface for the quantification, resulting in a lower degree of invasiveness and higher spatiotemporal resolution.[6] Nonetheless, electrochemical DA poses a number of challenges due to the large presence of interferent species in the extracellular fluid (such as ascorbic acid and uric acid) as well as DA metabolites (i.e., epinephrine, norepinephrine, 3-metoxytiramine – 3-MT, homovanillic acid – HVA, and 3,4- Dihydroxyphenylacetic acid – DOPAC) that can hinder the detection, since they exhibit electrochemical features similar to those of DA.[7–9] Electrochemical techniques are based on faradic processes, hence they systematically suffer from a loss in electrode functioning over time, caused by degradation of the electrode interface upon subsequent operations, and from electrode biofouling.[10,11]

Aiming at designing a new route for the in vivo quantitative determination of DA, it is possible to exploit the peculiar features of organic neuromorphic electronics. It exploits Organic Mixed Ionic-Electronic Conductors – OMIECs – with their biocompatibility, cycle stability, coupling between ionic and electronic currents– and, specifically, their response upon frequency-encoded biasing.[12,13] Such modes of operation give rise to transient or permanent changes in OMIECs electrical parameters that resemble the plasticity phenomena observed in real neurons and synapses. Following this suggestive analogy, these phenomena are termed short-term plasticity (STP) and long-term plasticity (LTP). Plasticity phenomena in organic electronic neuromorphic systems are ultimately caused by permanent or transient alteration of the ionic equilibria in close proximity to the OMIEC, therefore, they can be used to store memory[14] and detect variations of the electrolytic environment in which the device operates.[15,16]

Among OMIECs exhibiting neuromorphic features, poly(3,4-ethylenedioxythiophene):polystyrene sulfonate (PEDOT:PSS) was demonstrated in 2-terminal architectures (i.e., organic artificial synapses), as well as in 3-terminal architectures (i.e.,

electrolyte-gated organic transistors) that enable different ways to achieve operational control and tuning of plasticity phenomena.[17–20] This resulted in the definition of a novel toolset of device figures of merit, related to their time/frequency dependent response, and suitable to classify the device not only in terms of resistive and capacitive contributions but also referring to electrochemical pseudo-inductances, accounting for the kinetically stored energy at the OMIEC interface. This set of descriptors enables multiparametric neuromorphic sensors with the potential to be translated in vivo.[21]

STP-based paradigms for DA sensing were demonstrated in the case of bench-side DA sensing in model solutions with organic artificial synapses reaching high sensitivity and specificity also in the presence of interferent species and DA metabolites.[22–24]

In this work, we propose a way to translate such approaches in vivo, while minimizing their invasiveness, by developing a Single Electrode Neuromorphic Device (SEND) aimed at in vivo monitoring of DA by means of its neuromorphic response. We discuss its simple fabrication and investigate systematically its multiparametric dependency on operational frequency. The SEND shows high cycle stability (>7 h of repetitive operation) both at the bench-side in complex fluids (such as the artificial cerebrospinal fluid – aCSF) and in vivo implanted in the rat brain, where it allows real-time detection and spatial mapping of physiological extracellular DA levels.
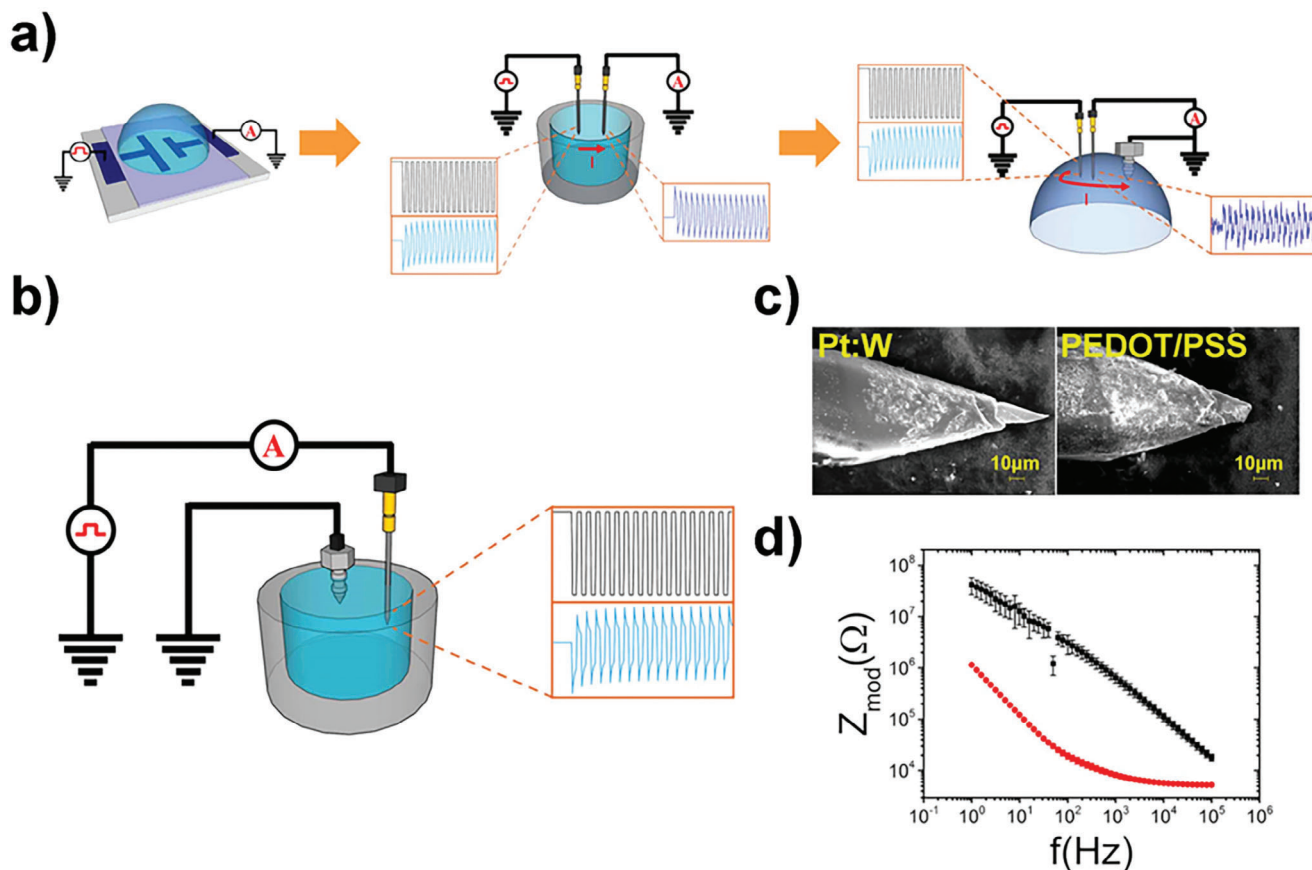
2. Results and Discussion

2.1. System Design and Translation

The development process leading to SEND design is schematically described in **Figure 1a**.

The starting architecture was a 2-terminal layout achieved by patterning two PEDOT:PSS terminals (namely, the pre-synaptic and the post-synaptic one) onto a polymeric substrate. Such design, whose sensitivity and specificity toward DA was discussed elsewhere,[22,24] is driven with a square voltage wave at the pre-synaptic electrode while recording the post-synaptic current at the other terminal (Figure 1a, left).

The first step toward translation of such architecture requires the miniaturization of the very same layout, moving from a flat surface to two deep-brain fiber electrodes covered by electrode-posited stoichiometric PEDOT/PSS (Figure 1a, center).[21] It is important to notice that both the driving pre-synaptic voltage and the post-synaptic depressive current are applied/recorded with respect to an external ground reference, which is not in contact with the operational electrolyte. This is not the case when performing an in vivo experiment, since the surgical context demands the compresence of other electrical references (typically, at least a ground reference) that exhibit much lower interfacial impedance with respect to the post-synaptic recording electrode. In this situation, current elicited by the pre-synaptic voltage driving preferentially flows to the ground and, as a consequence, the post-synaptic terminal records only noise (Figure 1a, right). Importantly, using source-measure units to drive artificial synapses allows us to acquire the pre-synaptic current. In the absence of ground or reference electrodes, pre-synaptic and post-synaptic currents are – quite obviously – equal and opposite, as shown

**ADVANCED
SCIENCE NEWS**

www.advancedsciencenews.com

**ADVANCED
ELECTRONIC
MATERIALS**

www.advelectronicmat.de

Figure 1. a) SEND development, from a two-terminal bench-side flat organic artificial synapse to an implantable organic architecture. Insets show input (solid black lines) and output (solid blue lines) signals; b) Final schematics of the implantable SEND with details on the provided input voltage (solid black line) and recorded output current (solid blue line); c) Scanning electron microscopy micrograph of the SEND tip in pristine condition (left) and after electrodeposition (right); d) Comparison of the Bode-plots of electrochemical impedance spectroscopies on the SEND in pristine (black squares) and PEDOT/PSS coated (red circles) conditions (N = 10, standard deviation as error bars).

in Figure S1 (Supporting Information), which presents a summary of pre- and post- synaptic currents in all the architectures depicted in Figure 1a.

This current mirroring is the main conceptual justification that allows us to move from the artificial synapse to the proposed SEND, Figure 1b. In SEND, the square wave is administered at the fiber electrode, while recording the STP response of the current between the SEND itself and the ground reference. As discussed, albeit with an opposite sign, this current conveys the exact same information as the post-synaptic one in two-terminal architectures, thus its multi-parametric evolution can be used as sensing observable. In terms of fabrication, SENDs can be obtained via the same procedure discussed for two-terminal implantable artificial synapses,[21] namely coating the tip of a quartz-insulated Pt:W deep-brain electrode via potentiostatic electrodeposition of PEDOT/PSS, as discussed in detail in the Experimental section.
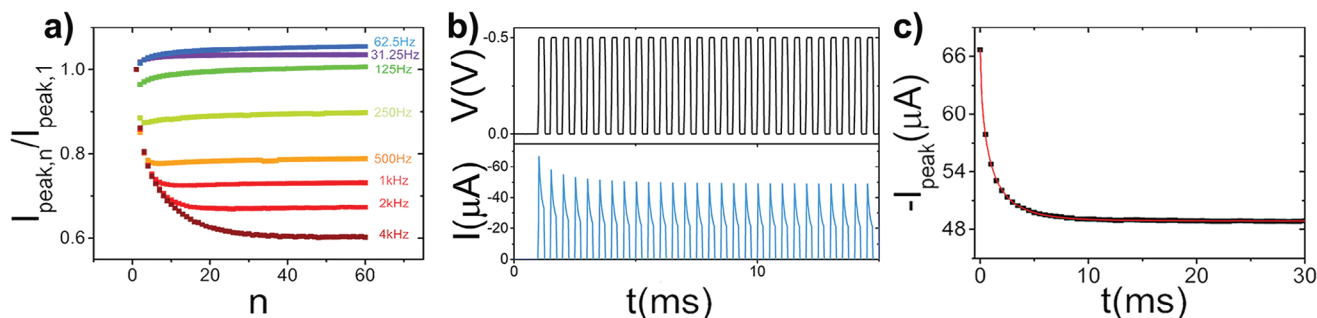
Efficiency of the coating procedure can be assessed by means of scanning electron microscopy (SEM) (Figure 1c), energy dispersive X-ray spectroscopy (Figure S2, Supporting Information), and electrochemical impedance spectroscopy (EIS, Figure 1d), from which it is possible to appreciate the typical impedance de-

crease subsequent to PEDOT/PSS deposition correlated to an increase of the electroactive surface area.[25–27]

2.2. Frequency-Dependent STP Response of SEND

Aiming at the determination of optimal operational frequency for SEND, its STP response to square voltage waves at different frequencies (i.e., 31.25 Hz, 62.5 Hz, 125 Hz, 250 Hz, 500 Hz, 1 kHz, 2 kHz, 4 kHz) was investigated in aCSF. This medium (see Experimental Section) contains also non-electrolytic moieties and it is enriched in monovalent and divalent cations, thus better resembling the physiological composition of the brain extracellular fluid, if compared to the commonly used phosphate-buffered saline solution (PBS). Figure S3 (Supporting Information) shows a 3D I versus t versus frequency plot of the investigated STP responses.

A qualitative comparison between the STP responses at different driving frequencies is shown in **Figure 2a**, which reports the negative peaks of each current trace at the *n-th* spike, $I_{peak,n}$, normalized over the first current peak, $I_{peak,1}$, versus the spike number, *n*. STP dependence on frequency in aCSF follows the

**ADVANCED
SCIENCE NEWS**

www.advancedsciencenews.com

**ADVANCED
ELECTRONIC
MATERIALS**

www.advelectronicmat.de

Figure 2. a) Normalized SEND peak currents at different operational frequencies versus the pulse number n, enabling qualitative comparison between STP responses; b) Driving voltammogram (top panel) and resulting output current (bottom panel) at the chosen frequency f = 2 kHz; c) Fit of the peak current amplitudes according to Equation 1, showing excellent representation of the experimental data.

same trend already reported for PBS electrolytes. In particular, while moving from high to lower frequencies, the STP response changes from purely depressive (i.e., exhibiting a monotonic decrease of the current peaks upon pulsing) to mildly facilitating (i.e., exhibiting a monotonic current peak increase upon pulsing). Depressive response is dominant at higher frequency (500 Hz<f<4 kHz) while it is possible to observe a gradual shift to purely facilitative behavior (31.25Hz<f<125 Hz), passing through an intermediate frequency range in which the two phenomena co-exist (125Hz<f<500 Hz).

DA sensitivity and specificity of PEDOT:PSS-based neuromorphic sensing architectures arise from the higher retention time of DA inside PEDOT:PSS, in a condition of purely depressive STP device response.[22] In this work, as a consequence, the lowest operational frequency capable of eliciting purely depressive response (2 kHz) has been selected for in vivo operations with SEND. The typical SEND response to 2 kHz voltage drive is shown in Figure 2b. Envelope of the extracted peaks can be fitted with Equation 1 in order to obtain descriptors of the STP response:

$$-I_{peak}\ (t) = I_{\infty} + \Delta I e^{-\left(\frac{t}{\tau_{STP}}\right)^{\beta}} \tag{1}$$

In the stretched exponential Equation 1, $-I_{peak}(t)$ is the opposite of the peak current as a function of time, I_{∞} is the current plateau achieved upon pulsing, ΔI is the STP amplitude (namely the maximum achievable current depression), τ_{STP} is the characteristic time of the depressive response (i.e., the time after which the current decreases to the value $I_{\infty} + \frac{\Delta I}{e}$), and β is the stretching exponent, accounting for disorder phenomena arising from repetitive perturbation in the PEDOT:PSS – electrolyte system.[28,29] Figure 2c shows good agreement of the fit with the experimental data for the STP of Figure 2b.

## 2.3. Stability Assessment of the STP-Driven SEND

When aiming at continuous DA monitoring in vivo, temporal stability of the sensing interface is critical for obtaining reliable quantitative parameters. Stability was assessed as follows: SENDs were repetitively operated as described above, collecting a 2kHz-STP response each 10s for a total time up to nine hours in aCSF, using a surgical stainless-steel screw as ground reference. **Figure 3a** shows the experimental setup for stability assessment in aCSF, with SEND already mounted on the stereotaxic apparatus used for in vivo electrophysiology. In Figure 3b, which shows the time evolution of all the parameters extracted from Equation 1, it is possible to appreciate how τ_{STP}, β, I_{∞}, and ΔI – after an initial stabilization phase lasting roughly 1 h – remain constant up to 6.5 h of repetitive operation.

By means of EIS (Figure 3c) it is possible to check the integrity of the film after the temporal stability assessment, unveiling the absence of significant electrically-induced damage or performance variation of SENDs upon repetitive operation. Nonetheless, other sources of potentially harmful stress can compromise SEND performances during an intra-cortical experiment. First and foremost, the brain tissue opposes a drastically higher resistance to electrode piercing with respect to an electrolytic solution. Therefore, it is necessary to evaluate the possibility of mechanical damage to the PEDOT/PSS coating of SENDs upon neural tissue piercing. For this purpose, a simple model of the mechanical features of brain tissue was used, building a "phantom brain" with an aCSF-based agarose gel,[30] as described in the experimental section, and the measurement was carried out by piercing it with SENDs, with steps of 300 µm every 15 min thanks to a micro-advancer (see Experimental Section). This enables to study the parameter evolution as a function not only of time but also of piercing depth.

Photograph of the actual setup, parameters evolution versus time and versus piercing depth, as well as before/after EIS for this experimental setup are reported in Figure 3d–f, respectively.

Apart from demonstrating SEND's excellent stability in the operational context (>1800 cycles, >6 h), which exceeds that of standard PEDOT:PSS OECTs[31] and compares to the record one of PEDOT-S:(Oct)$_2$NH$_2$ ones,[32] this comparison enables us to draw some important conclusions on the chemo-physical origin of the STP parameters. First of all, the value of the stretching exponent β is closer to unity in the phantom brain with respect to aCSF, hinting at less dynamical electrical double layers even in the same ionic environment. This suggests that β relates to the non-ion-dependent parameters determining the STP response (e.g., medium density, temperature, etc.). The parameters τ_{STP}, and ΔI converge to comparable values in aCSF and in the phantom brain, remaining almost unaffected by the piercing, while I_{∞} shows a moderate increasing trend upon piercing, which cannot be observed in aCSF. In both cases, the variation of
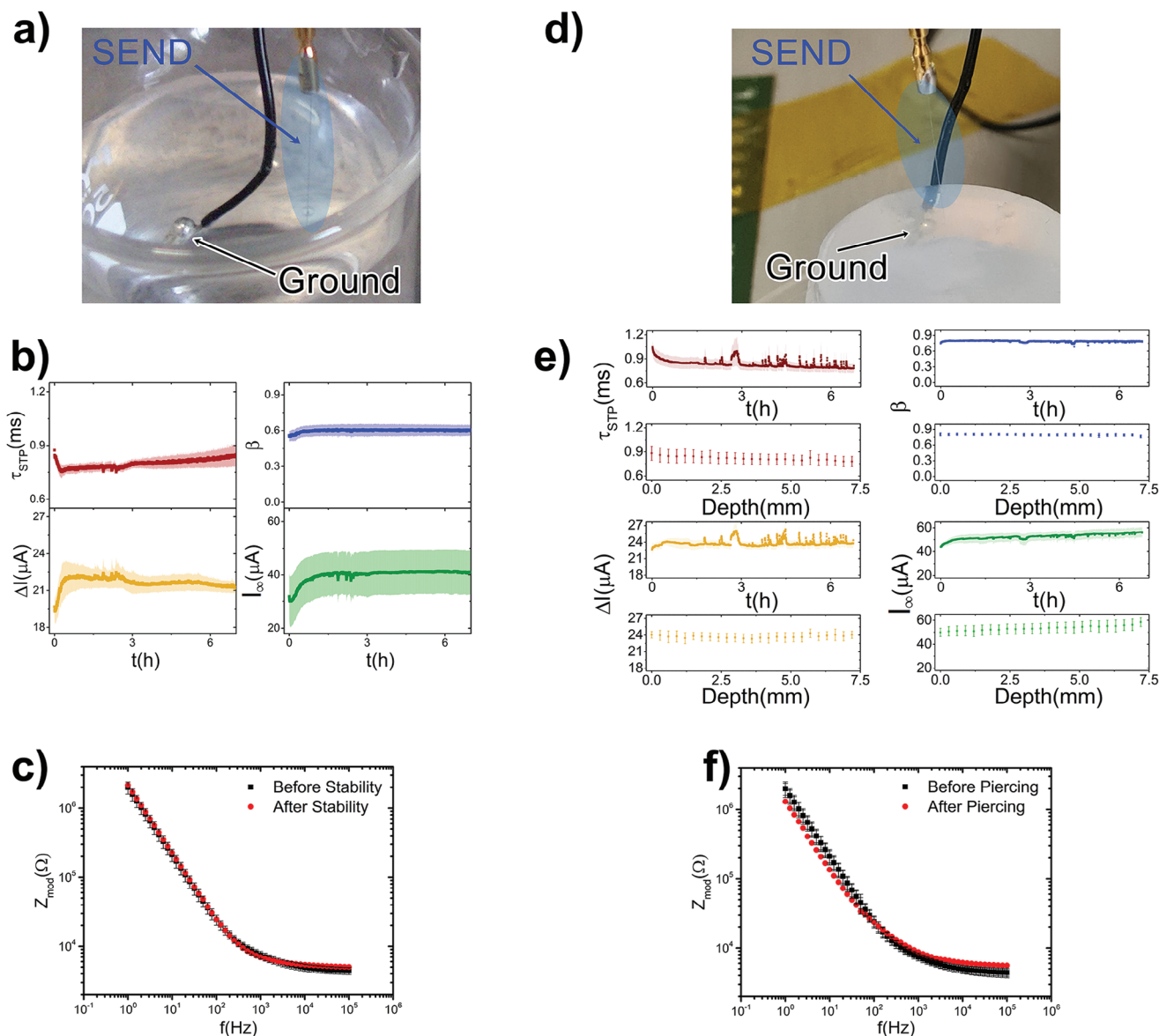
Figure 3. a) Photograph of the experimental set up for stability characterization in aCSF; b) time-evolution of the fitting parameters in aCSF (N = 3, standard error of the mean as error bars); c) EIS characterization before and after the stability experiment in aCSF (N = 3, standard deviation as error bars); d) Photograph of the experimental set up for stability characterization in the phantom brain; e) evolution of the fitting parameters as a function of both time (top panels) and piercing depth (bottom panels) during phantom brain piercing (N = 3, standard error of the mean as error bars). f) EIS characterization before and after the stability experiment in phantom brain (N = 3, standard deviation as error bars).
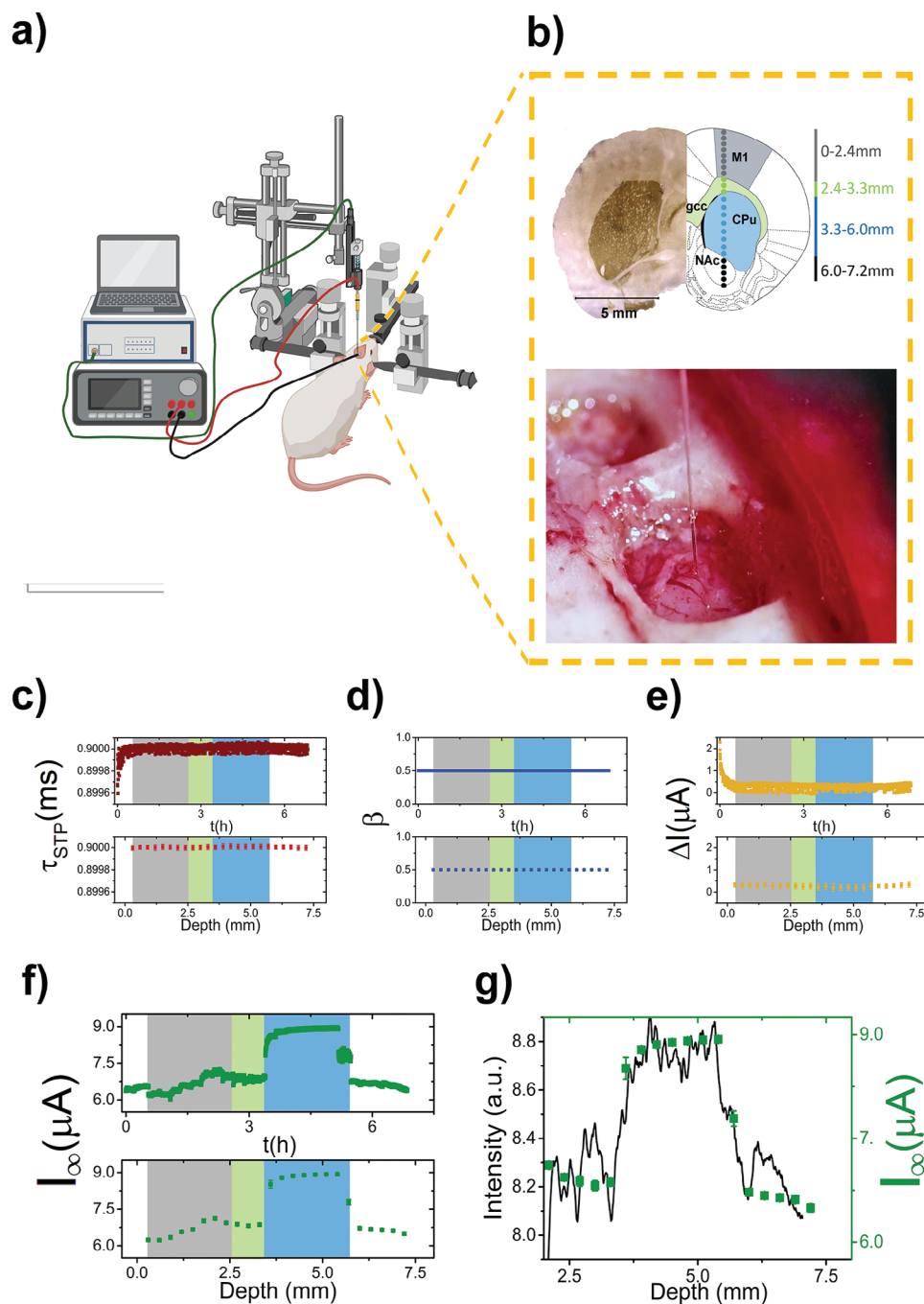
the impedance spectra after 6.5 h of repetitive operation is negligible.

2.4. Detection of Physiological DA with In Vivo-Operated SEND

As a final validation, SENDs were implanted in rat brains, repeating the piercing experiment described in Section 2.3. **Figure** 4a schematically depicts the experimental layout, with emphasis on the micro-advancer and the stereotaxic apparatus, which guarantee precise positioning, and on the Source-Measure Unit used for SEND driving and data acquisition. The selected piercing

pathway, shown in Figure 4b, ensures that the main chemophysical variation of the environment lies in the extracellular DA concentration.[33]

Rats are anesthetized, and a standard surgical procedure is performed to expose the rat motor cortex (M1), removing both the scalp and the dura mater of the rat. The micro-advancer moves the device inside the brain along the dorso-ventral axis with steps of 300 μm (measuring sites highlighted as solid dots in Figure 4b), and is kept still for 15 min for each measuring site. The piercing pathway starts from M1 (grey-shaded region in Figure 4b), crosses the *corpus callosum* (*gcc*, green-shaded region in Figure 4b), then penetrates the CPu

2400467 (5 of 9)

**ADVANCED
SCIENCE NEWS**

www.advancedsciencenews.com

**ADVANCED
ELECTRONIC
MATERIALS**
Open Access

www.advelectronicmat.de

Figure 4. a) Schematic representation of the in vivo SEND evaluation showing the overall experimental setup b) Experimental design of the in vivo piercing experiment, highlighting Measurement points as reconstructed onto schematic templates of coronal sections (adapted from[28]) (top right), histology of the brain at the experimental coordinates (top left) and optical micrograph of an implanted SEND (bottom); c) Time- and depth-profile of τ_{STP} in vivo; d) Time- and depth-profile of β in vivo; e) Time- and depth-profile of ΔI in vivo; f) Time- and depth-profile of I_∞, showing in vivo DA mapping. g) Comparison of optical intensity (left axes), from the histological evaluation, and I_∞ (right axes), from SEND profiles versus piercing depth.

(blue-shaded region in Figure 4b) and terminates in the NAc (unshaded region in Figure 4b). The M1 extracellular[DA] is reported (from micro-dialysis studies[34–37]) to be ≈50 times lower than that of CPu. In particular, along the piercing pathway,[DA] passes from ≈250pM in M1, up to ≈20 nM in the CPu and back to ≈4 nM in NAc. Figure 4b shows also

the corresponding coronal section after selective staining for tyrosine-hydroxylase, a marker for the presence of dopaminergic neurons, and a micrograph of the actual SEND implantation site.

Figure 4c–f shows the spatio-temporal evolution of τ_{STP}, β, ΔI and I_∞ along the piercing pathway, respectively, as extracted

from the fitting procedure (Figure S4b, Supporting Information, shows examples of STP responses in the different brain regions).

As expected from the stability studies of Figure 3, τ_{STP}, β, ΔI (Figure 4c–e) are substantially unaffected throughout the piercing experiment, apart from their initial stabilization phase, while I_∞ shows a slowly increasing trend as the one observed in the phantom brain upon piercing. Moving from gcc to CPu shows a clear discontinuity (i.e., it exhibits a 30% increase, changing from 6.86 to 8.93 µA) as a consequence of the 20-fold increase of [DA].[34] I_∞ returns to baseline levels when moving from CPu to NAc and, hence, can be regarded as the DA-sensitive parameter of the proposed SEND, conversely to what happens in two-terminal bench-side architectures, where mainly τ_{STP} is DA-sensitive.[24]

This difference is not surprising since, at the proposed operational frequency of 2 kHz (which is necessary to elicit purely depressive STP in the miniaturized architecture), it is impossible to sample the timescales of DA intake/release by the PEDOT/PSS, which constitutes the conceptual core of artificial synapse-based DA detection but is too slow for SENDs. This inevitably results in the fact that the ionic motion causing STP in SENDs at 2 kHz involves faster carriers (i.e., protons or small monovalent cations in the electrolyte). In this situation, it is still possible to use the STP response of SEND to collectively monitor the number of displaceable cations upon repetitive voltage pulsing thus, by difference, gaining information on the number of cation-accessible sites in the SEND, which is a qualitative estimate of the effective capacitance of SEND upon negative voltage driving. The observed I_∞ increase upon [DA] increase, given the extreme stability of τ_{STP}, β and ΔI, can be ascribed solely to the presence of a higher effective capacitance in the CPu with respect to the other investigated regions, which causes higher I_{peak} and, subsequently, higher I_∞ (Figure S4a, Supporting Information). The origin of such an increase of effective capacitance in the presence of increased DA may arise from the geometrical and energetic rearrangement of the PEDOT/PSS-electrolyte interface, which are known to be affected by DA binding more than by any of its catabolites or interferents.[22] Indeed, when moving from gcc to CPu, part of the extracellular cationic DA slowly binds (≈20 min, Figure 4f, top panel) to the PEDOT/PSS, giving rise to the observed I_∞ increasing trend. Clearly, this partition equilibrium is reverted when going from CPu to NAc, and I_∞ returns to its basal value.

It is important to notice that SEND cannot discriminate between NAc and M1 in terms of [DA]. This could be due either to non-linear sensor response or to a sensitivity limit higher than 4 nm (i.e., [DA] in NAc). In both cases, the diagnostic utility of SEND-based [DA] mapping is conserved, since its dynamic range seems to be centered near the transition between high 10^{-9} M and low 10^{-8} M, which is exactly the range of [DA] variations that are not accompanied by glaring motor symptoms.

Figure 4g shows an overlay between the I_∞ trend (green scatter) and the intensity profile (black solid line) extracted by the negative of the histological image reported in Figure 4b (Figure S5, Supporting Information), both reported here as a function of depth. Details on image analysis are provided in the Experimental Section. The extremely good accordance (Pearson's correlation coefficient = 0.779) between these two orthogonal observables, both related to DA local concentration, is further evidence of the suitability of the proposed approach to achieve effective DA mapping in vivo.

3. Conclusion

This work describes the mono-electrode neuromorphic unit – SEND – as a viable tool for translating the STP-based DA sensing paradigm based on two-terminal artificial synapses to in vivo context. The resulting architecture is a fiber electrode featuring an electrodeposited PEDOT/PSS thin film on its sharp tip as active interface, thus reducing system dimensionality system and compressing the concept of organic artificial synapse to a mono-electrode device. SENDs show good stability upon repetitive voltage pulsing for more than 6.5 h in aCSF, in phantom brain models and in the rat brain.

The multi-parametric analysis of STP response gives insights on non-ion-dependent phenomena (embedded in the stretching exponent – β), and ion dependent dynamics (embedded in the plateau current – I_∞ – at the selected operational frequency).

SEND's detection strategy, which rely on displacement current related to the intake/release of molecules at the SEND interface, envisions the possibility to achieve physiological DA monitoring without the involvement of faradic-processes increasing the durability of the sensor upon cycling and, ultimately, the safety of the implant.

4. Experimental Section

Chemicals: A solution of EDOT (3,4-Ethylenedioxythiophene, 0.01 M) and NaPSS (sodium polystyrene sulfonate, 0.7% w/w) is used for the PEDOT/PSS electrodeposition, as described below. The artificial cerebrospinal fluid (aCSF) used to investigate the time-/frequency- response and the stability over time of SENDs is a 127 mM NaCl, 1 mM KCl, 1.2 mM KH_2PO_4, 26 mM $NaHCO_3$, 10 mM D-glucose, 2.4 mM $CaCl_2$, 1.3 mM $MgCl_2$ aqueous solution at pH 7.4.

SENDs Fabrication, Electrodeposition, and Characterization: The proposed architecture involves a fiber electrode (Thomas RECORDING GmbH) featuring a metal core constituted by 96% of platinum (Pt) and 5% of tungsten (W, diameter of 25 µm) insulated by 55 µm quartz glass, for a final diameter of 80 µm of diameter.

To expose the metal core in a sharp Pt:W tip (tip lateral surface ≈ 2 × 10^{-5} cm^2), the fiber electrode is grinded by means of a grinding machine, purchased by Thomas Recording GMBH, with the shape of a sharp conductive Pt:W tip.

The exposed tip is coated with a PEDOT/PSS thin film via potentiostatic electrodeposition in charge control (V = 0.85 V, charge = 2.5 µC, final charge density = 125 mC cm^{-2}, pre-conditioning the fiber electrode at 0.2 V for 5 s) in a two-terminal electrochemical cell using a platinum mesh as the counter electrode.

Electrochemical impedance spectroscopy (amplitude = 10 mV, 1 Hz < frequency < 100 kHz) is performed in aCSF, as described above.

Both electrochemical impedance spectroscopy and electrodeposition are performed with a Gamry Reference 600 potentiostat/galvanostat (Gamry Instruments).

Scanning Electroni Microscopy (SEM) and Energy Dispersive Spectroscopy (EDS): SEM and EDS information are acquired using a Zeiss SEM EVO400.

For the imaging the instrument is operated with an accelerating voltage of 10 keV and a probe beam current of 10pA under high vacuum (5.33 × 10^{-7} mBar<Pressure←6.66 × 10^{-7} mBar) using secondary electrons as signal.

Differently, for EDS the instrumentation is operated in the same vacuum but with a current of 1nA and with an objective/sample working

**ADVANCED
SCIENCE NEWS**

www.advancedsciencenews.com

**ADVANCED
ELECTRONIC
MATERIALS**
Open Access

www.advelectronicmat.de

distance of 9–9.5 mm collecting the X ray signals upon the collision of primary electrons with the samples.

The samples used for SEM imaging are Au coated by means of a Mini Sputter Coater/Glow Discharge System SC7620 (Quorum technologies) sputtering 20 nm of Au with a current 18 mA for 120s keeping the system under vacuum (6×10^{-2} mBar) while non coated samples are used for EDS.

STP Characterization and Stability Experiments: The SEND is operated in aCSF providing square 60 pulses square waves of different frequencies, ranging from 31.25 Hz to 4 kHz, featuring an amplitude of −0.5 V and a duty cycle ½ recording the current at the very same electrode interface. Both the square wave administration and the current recording are done by means of a source/measure unit (Keysight B2912A) using a stainless-steel screw as ground reference.

For the stability experiment, the same layout mentioned before is used providing a square wave with the aforementioned characteristics at 2 kHz frequency recording the current. Then, the envelope of the current minima peaks is extracted and fitted with Equation 1.

The stability experiments are carried out in aCSF with a bathing ground stainless steel screw; to check the piercing resistance of the interface the very same experiment is carried out also in a gel phantom brain[30] prepared with aCSF added of 0.6% of agarose (jellification overnight room temperature).

In Vivo Mapping of DA in Rats: Three adults male Wistar rats (mean weight 250– 300 g), were used for piercing experiments to map physiological extracellular DA levels across different brain region with the SEND electrode. Rats used came from the animal facility of the University of Ferrara, where they were housed under regular lighting conditions (12 h light/dark cycle), as well as temperature (20–22 °C) and humidity (55–65%) ranges. The experimental protocol complied with the ARRIVE guidelines and the European Communities Council Directive of 24 November 1986 (86/609/EEC). and it was designed in compliance with Italian law regarding the care and use of experimental animals (DL26/2014), approved by the institutional review board of the University of Ferrara and the Italian Ministry of Health (permission n. 989/2020-PR). Adequate measures were taken to minimize animal pain as well as the number of animals, according to the three Rs principle.[38]

Rats were first administered with ketamine hydrochloride (80 mg kg^{-1}) for anesthesia. Throughout the session, further ketamine injections (4 mg kg^{-1}, given as needed, usually every 25–30 min) were utilized to maintain long-latency and slow hindlimb withdrawal upon pinching the hindfoot. Animals were placed in a Kopf stereotaxic apparatus (David Kopf Instruments, Tujunga, CA, USA), and a heat lamp maintained the body temperature at 36–38 °C. A craniotomy was performed under stereomicroscopy (Carl Zeiss Meditec AG, S100/OPMI pico, Jena, Germany) to expose a portion of the M1. The dura was removed and kept moist with saline solution.

The SEND was mounted on a microadvancer (Kopf Micropositioner 2650, David Kopf Instruments, Tujunga, CA, USA) and lowered perpendicularly (depth step of 300 µm from the cortical surface,) according to the following coordinates from the bregma: AP = +1.20 mm, ML = 2 mm.[33] At each step, a square wave was repeatedly delivered for 15 min during the brain piercing, with the beforementioned parameters (see previous paragraph). In the portion of skull caudal with respect to the craniotomy, a stainless-steel screw was implanted to serve as ground.

Histological Evaluation: At the end of the experimental sessions, the animals were deeply anaesthetized with Zoletil 100 (10 mg Kg^{-1}; Virbac Laboratories, Carros, France). The brains were first perfused with 20 mM potassium PBS (KPBS) and then fixed with 4% paraformaldehyde in KPBS (pH 7.4) overnight. After the exposure to the fixative agent the brains were removed and placed in a 25% sucrose added KPBS buffer for cryoprotection and Brain coronal sections at the experimental coordinates were made using a freezing microtome.

The coronal sections were then used to detect tyrosyne hydroxilase (TH) via an immunohistochemistry procedure, routinely used to highlight the presence of dopaminergic neurons.[39]

Treated coronal sections micrographs are then analyzed to extract the light intensity profile along the investigated piercing path, as a mean for the qualitative estimation of dopamine concentration. In particular, it is possible to obtain such profiles by arbitrarily assigning the value of 10 a.u. to a white pixel and the value of 0 a.u. to a black one. In order to remove adventitious noise, 128 adjacent profiles, corresponding roughly to a width of 0.9 mm and centered on the piercing coordinate have been averaged, resulting in the average intensity profile.

Data Analysis: All the presented data are analyzed using Matlab (version 9.10, Mathworks, Natick, MA, USA) for the extraction of the current peak envelopes and fitting while the plotting of data has been done using OriginPro2016. Optical images from histological evaluation are analyzed using Gwyddion 2.55. Figure panels are assembled in Adobe Photoshop CS6, 3D-device schematics are sketched in SketchUp Make 2017.

Supporting Information

Supporting Information is available from the Wiley Online Library or from the author.

Conflict of Interest

The authors declare no conflict of interest.

Data Availability Statement

The data that support the findings of this study are available from the corresponding author upon reasonable request.

[1] G. Ayano, *J. Ment. Disord. Treat.* **2016**, *2*, 2.
[2] L. Speranza, U. Di Porzio, D. Viggiano, A. de Donato, F. Volpicelli, *Cells* **2021**, *10*, 735.
[3] W. Oertel, J. B. Schulz, *J. Neurochem.* **2016**, *139*, 325.
[4] H. C. Cheng, C. M. Ulane, R. E. Burke, *Ann. Neurol.* **2010**, *67*, 715.
[5] K. Jackowska, P. Krysinski, *Anal. Bioanal. Chem.* **2013**, *405*, 3753.
[6] A. E. Rusheen, T. A. Gee, D. P. Jang, C. D. Blaha, K. E. Bennet, K. H. Lee, M. L. Heien, Y. Oh, *TrAC – Trends Anal. Chem.* **2020**, *132*, 116049.
[7] X. Liu, J. Liu, *View* **2021**, *2*, 1.
[8] S. L. Boschen, J. Trevathan, S. A. Hara, A. Asp, J. L. Lujan, *Front. Neurosci.* **2021**, *15*, 1.

**ADVANCED
SCIENCE NEWS**

www.advancedsciencenews.com

**ADVANCED
ELECTRONIC
MATERIALS**

www.advelectronicmat.de

[9] N. Delmo, B. Mostafiz, A. E. Ross, J. Suni, E. Peltola, *Sensors and Diagnostics* **2023**, *2*, 559.

[10] J. G. Roberts, L. A. Sombers, *Anal. Chem.* **2019**, *90*, 490.

[11] C. He, M. Tao, C. Zhang, Y. He, W. Xu, Y. Liu, W. Zhu, *Crit. Rev. Anal. Chem.* **2022**, *52*, 544.

[12] P. Gkoupidenis, N. Schaefer, B. Garlan, G. G. Malliaras, *Adv. Mater.* **2015**, *27*, 7176.

[13] B. D. Paulsen, K. Tybrandt, E. Stavrinidou, J. Rivnay, *Nat. Mater.* **2020**, *19*, 13.

[14] V. Parkula, M. S. Maglione, S. Casalini, Q. Zhang, P. Greco, C. A. Bortolotti, C. Rovira, M. Mas-Torrent, F. Biscarini, *Adv. Electron. Mater.* **2019**, *5*, 1.

[15] E. R. W. Van Doremaele, P. Gkoupidenis, Y. Van De Burgt, *J. Mater. Chem. C* **2019**, *7*, 12754.

[16] S. Yamamoto, G. G. Malliaras, *ACS Appl. Electron. Mater.* **2020**, *2*, 2224.

[17] M. Di Lauro, A. De Salvo, G. C. Sebastianella, M. Bianchi, S. Carli, M. Murgia, L. Fadiga, F. Biscarini, *ACS Appl. Electron. Mater.* **2020**, *2*, 1849.

[18] S. Desbief, M. di Lauro, S. Casalini, D. Guerin, S. Tortorella, M. Barbalinardo, A. Kyndiah, M. Murgia, T. Cramer, F. Biscarini, D. Vuillaume, *Org. Electron.* **2016**, *38*, 21.

[19] F. Rondelli, A. De Salvo, G. Calandra Sebastianella, M. Murgia, L. Fadiga, F. Biscarini, M. Di Lauro, *Neuromorphic Comput. Eng.* **2023**, *3*, 1.

[20] S. T. Keene, C. Lubrano, S. Kazemzadeh, A. Melianas, Y. Tuchman, G. Polino, P. Scognamiglio, L. Cinà, A. Salleo, Y. van de Burgt, F. Santoro, *Nat. Mater.* **2020**, *19*, 969.

[21] G. C. Sebastianella, M. Di Lauro, M. Murgia, M. Bianchi, S. Carli, M. Zoli, L. Fadiga, F. Biscarini, *Adv. Electron. Mater.* **2021**, *2100755*, 2100755.

[22] M. Giordani, M. Sensi, M. Berto, M. Di Lauro, C. A. Bortolotti, H. L. Gomes, M. Zoli, F. Zerbetto, L. Fadiga, F. Biscarini, *Adv. Funct. Mater.* **2020**, *30*, 2002141.

[23] M. Giordani, M. Di Lauro, M. Berto, C. A. Bortolotti, D. Vuillaume, H. L. Gomes, M. Zoli, F. Biscarini, *Proc. SPIE 9944, Organic Sensors and Bioelectronics IX* **2016**, 99440P.

[24] M. Giordani, M. Berto, M. Di Lauro, C. A. Bortolotti, M. Zoli, F. Biscarini, *ACS Sens.* **2017**, *2*, 1756.

[25] C. Boehler, M. Asplund, Proc. Annu. Int. Conf. IEEE Eng. Med. Biol. Soc. EMBS **2018**, 2018-July, 2202.

[26] M. Bianchi, A. De Salvo, M. Asplund, S. Carli, M. Di Lauro, A. Schulze-Bonhage, T. Stieglitz, L. Fadiga, F. Biscarini, M. Bianchi, A. De Salvo, S. Carli, M. Di Lauro, L. Fadiga, F. Biscarini, A. Schulze-Bonhage, T. Stieglitz, M. Asplund, *Adv. Sci.* **2022**, *9*, 2104701.

[27] A. Lunghi, A. Mariano, M. Bianchi, N. B. Dinger, M. Murgia, E. Rondanina, A. Toma, P. Greco, M. Di Lauro, F. Santoro, L. Fadiga, F. Biscarini, *Adv. Mater. Interfaces* **2022**, *9*, 01400413.

[28] D. C. Johnston, *Phys. Rev. B – Condens. Matter Mater. Phys.* **2006**, *74*, 184430.

[29] B. A. Snopok, O. B. Snopok, *NATO Sci. Peace Secur. Ser. A Chem. Biol.* **2018**, 233.

[30] Z. J. Chen, G. T. Gillies, W. C. Broaddus, S. S. Prabhu, H. Fillmore, R. M. Mitchell, F. D. Corwin, P. P. Fatouros, *J. Neurosurg.* **2004**, *101*, 314.

[31] M. Xie, H. Liu, M. Wu, C. Chen, J. Wen, L. Bai, J. Yu, W. Huang, *Org. Electron.* **2023**, *117*, 106777.

[32] E. Zeglio, J. Eriksson, R. Gabrielsson, N. Solin, O. Inganäs, *Adv. Mater.* **2017**, *29*, 1605787.

[33] G. Paxinos, C.-T. Watson, The Rat Brain in Stereotaxic Coordinates, 2nd ed., **1996**.

[34] M. Shou, C. R. Ferrario, K. N. Schultz, T. E. Robinson, R. T. Kennedy, *Anal. Chem.* **2006**, *78*, 6717.

[35] L. H. Parsons, J. B. Justice, *J. Neurochem.* **1992**, *58*, 212.

[36] P. W. Awenowicz, L. L. Porter, *J. Neurophysiol.* **2002**, *88*, 3439.

[37] T. Aubele, M. F. Kritzer, *Cereb. Cortex* **2011**, *21*, 222.

[38] W. M. Russel, R. L. Burch, The Principles of Humane Experimental Technique. : Universities Federation for Animal Welfare, Universities Federation For Animal Welfare, Wheathampstead, UK **1959**.

[39] M. Marti, C. Trapella, R. Viaro, M. Morari, *J. Neurosci.* **2007**, *27*, 1297.